Ultra-high surface area and mesoporous N-doped carbon derived from sheep bones with high electrocatalytic performance toward the oxygen reduction reaction

Shunxi Li[1], Ruoyu Xu[2], Hui Wang[1], Dan J. L. Brett[2], Shan Ji[1,2*] Bruno G. Pollet[3] and Rongfang Wang[1*]

1. College of Chemistry and Chemical Engineering, Northwest Normal University, Lanzhou 730070, China

2. Department of Chemical Engineering, University College London, London, WC1E 6BT, England, UK

3. Power and Water, Swansea SA6 8QR, Wales, UK

Abstract: A nitrogen (N)-doped mesoporous carbon material exhibiting ultra-high surface area was successfully synthesized from sheep bones via a facile and low-cost method. The obtained carbon material had an ultra-high specific surface area of 1,961 m^2 g^{-1} and provided rich active sites for the Oxygen Reduction Reaction (ORR), which in turn resulted in high electrocatalytic activity. It was found that the pore size distribution for the newly prepared carbonaceous material fell in the range of 1-4 nm. Benefiting from its high surface area and the presence of pyridine-*N* and quaternary-*N* species, the *as*-prepared carbon material exhibited excellent ORR activity in an oxygen-saturated 0.1 M KOH solution, compared to commercial Pt/C (10 wt%). Due to its high ORR catalytic activity, stability and low-cost, using sheep bone as C and N

R.F. Wang (*): wrf38745779@126.com, S. Ji (**): jissshan@126.com.

precursors to produce N-doped carbon provides an encouraging step towards the goal of replacing commercial Pt/C as fuel cell cathode electrocatalyst.

Keywords: Ultra-high surface area; *N*-doped carbon; sheep bone; oxygen oxidation reaction.

Introduction

Cathodic electrocatalysts towards the oxygen reduction play a critical role in numerous promising renewable energy technologies, for instance, fuel cells and metal-air batteries [1-3]. Usually, carbon supported platinum (Pt/C) based electrodes are currently the state-of-art catalyst for catalyzing the four-electron Oxygen Reduction Reaction (ORR) [4,5]. However, the high price and scarcity of platinum hinder the successful deployment and applications of fuel cell and metal-air battery systems. Considerable efforts have focused on developing non-platinum catalysts of comparable performance to Pt-based catalysts from cost-effective and abundant starting materials [6-8]. In the search for low-cost noble-metal free ORR catalysts, various *N*-doped carbon materials have shown promising ORR electrocatalytic performance in alkaline media [9-11].

Generally, nitrogen doped carbon materials can be prepared by either directly doping, namely direct pyrolysis nitrogen containing precursors or post-doping, for instance post-treatment of carbon materials with nitrogen containing chemicals, such as NH_3 [12]. For example, Rühle *et al* [13] prepared aligned *N*-doped carbon nanotube (CNT) by pyrolysis of ferrocene/C_{60} under NH_3 atmosphere and found that the use of

ammonia is an effective way for obtaining high level of nitrogenation of carbon materials. Rao *et al* [14] showed that good quantities of aligned N-doped nanotube bundles could be produced by the pyrolysis of pyridine over cobalt or iron catalyst surfaces. Mokaya *et al* [15] reported that aligned *N*-doped carbon materials could be produced on zeolite substrate, using ferric nitrate as catalysts and acetonitrile as the carbon and nitrogen precursors over the temperature range 700-800 ^{o}C.

Mesoporous *N*-doped carbon materials were also developed due to their unique electronic properties, good mechanical/thermal stability, excellent electrochemical performances and mesoporous networks [16]. Mesoporous N-doped carbon materials were prepared by using di-cyanamide-containing IL 3-methyl-1-butylpyridine dicyanamide as precursors and 12 nm SiO_2 nanoparticles as template at 900 °C, and followed by the removal of SiO_2 template [17]. N-doped mesoporous carbon materials can also be synthesized via a nano-casting process using polyacrylonitrile as nitrogen and carbon sources and mesoporous silica SBA-12 as hard template [18]. Yi *et al* [19] reported that mesoporous N-doped carbon may be prepared using mesoporous silica as a template and sucrose as a carbon source, and followed by ammonization at high temperature. However in most cases, the used nitrogen containing precursors are expensive and the post-doping pyrolysis procedures are too complicated to be industrially scaled-up for commercial applications. Therefore, there is an urgent challenge to develop alternative mesoporous N-doped carbon materials with excellent electrochemical performance but without the use of expensive precursors and complicated production procedures.

Biomass containing large amounts of proteins and amino acids is a promising precursor for producing N-doped carbon materials. For example, world lamb consumption increased from 6 billion kg in 1965 to 10 billion kg in 2011 (http://www.agmrc.org/commodities-products/livestock/lamb/international-lamb-profile/). Lamb bone materials are a by-product in the lamb production, which could potentially be used as low cost raw materials for producing N-doped carbon materials.

In this work, we developed a facile, low-cost and scalable method to prepare mesoporous N-doped carbon exhibiting ultra-high surface area from lamb bone starting material. We found that the *as*-synthesized N-doped carbon contains abundant mesopores of ultra-high surface area, resulting in higher electrocatalytic activity toward the ORR in alkaline medium, when compared to commercial Pt/C (10%) catalyst.

Experimental

Synthesis: The detailed procedure for preparing nitrogen doped carbon material from sheep bone starting material is as follows: sheep bones were washed with detergent to strip oil off of the surface, and rinsed with tap water. The dried bones were dried in a vacuum oven at 80 ^{o}C. The dried sheep bones were ground thoroughly and vigorously into a fine powder using a ball-miller. The samples were pre-carbonized under nitrogen atmosphere at 450 ^{o}C for 2 h. Then the pre-carbonized bones were mixed with potassium hydroxide (KOH) with a weight ratio of 1:1 and placed in a quartz tube furnace and carbonized to 850 ^{o}C under nitrogen atmosphere for 2 h. The obtained product was immersed in a 2 M HNO_3 solution for 24 h to remove any traces

of inorganic compounds, such as calcium compounds (present in the bones), and then dried in a vacuum oven at 80 ^{o}C for 12 h.

Characterization: X-ray diffraction (XRD) patterns of the materials were obtained using a Shimadzu XD-3A (Japan) and a CuKα radiation operating at 40 kV and 30 mA. Scanning Electronic Microscope (SEM) images were generated using a JSMF-6701F (JEOL Co., Japan) operating at 5 kV. Raman spectroscopy was carried out using a FT-Raman spectroscopy (RFS 100, BRUKER) with a Nd:YAG laser (λ = 1064 nm). The surface area was calculated using the nitrogen adsorption and the Brunauer-Emmett-Teller (BET) method, and the pore size distribution was calculated from the isotherms using the Density Functional Theory (DFT) procedure. X-ray Photoelectron Spectra (XPS) was obtained from a VGEscalab210 spectrometer fitted with a Mg 300 W X-ray source. Binding energies were determined by referencing to the C 1*s* peak at 285.0 eV. The elemental analysis of C and N elements were conducted using an organic elemental analyzer (Thermo Flash2000).

Electrochemical measurements: Electrochemical measurements were carried out using an electrochemical workstation (potentiostat/galvanostat CHI650D, Shanghai Chenhua Co., China). A three-electrode electrochemical cell was used for the measurements. The counter (CE) and reference electrodes (RE) were a platinum wire and an Ag/AgCl (saturated KCl solution) electrode respectively. A Rotating Disc Electrode (RDE) was used as the working electrode (WE), which was prepared as follows: 5 mg of the electrocatalyst was dispersed ultrasonically in 1 mL Nafion®/ethanol (0.25% Nafion®) and 8 µL of the dispersion was carefully

transferred onto the glassy carbon disc (∅ = 5 mm) using a pipette and then dried in air.

Results and discussion

The morphology of carbon materials made from sheep bone starting materials was investigated by SEM analyses as shown in Figure 1. It was found that the particle size distribution of the Carbonized Sheep Bones (CSB) was in the range of 500-1,000 nm. As shown in Figure 1a, the sheep bones which were not mixed with KOH and carbonized at 850 ^{o}C exhibited a rock-like morphology. However, after the sheep bones were mixed with KOH and then carbonized at high temperature (850 ^{o}C), it was found that the particle sizes were much smaller than those observed for CSB. It was observed that the CSB material contained many irregular honeycomb-like pores, revealing a porous structure that was formed after chemical and heat treatment. The structure of the CSB was also characterized by TEM. The TEM image in Figure 1c reveals an irregular morphology with plenty of edges and borders between the particles. Moreover, no other heterogeneous particles were observed in the synthesized material. As can be seen in Figure 1d, high-resolution TEM images reveal the existence of graphitic planes in the CSB samples.

Raman spectroscopy on CSB and Vulcan XC-72 carbon materials (Figure 2) was carried out to observe the degree of structure defect and the chemical structure of the materials. Raman spectra of CSB and Vulcan XC-72 carbon materials show two peaks at ~1,300 and ~1,587 cm^{-1}, corresponding to the Raman active *D* band and *G* band, respectively [20]. The *D*-band corresponds to the atomic disorder and the

displacement caused by lattice distortion, defect, and the *G*-band is attributed to all sp^2 bonds of the graphitic network [21]. The extent of the defects can be quantified by the ratio of the I_D/I_G in graphite materials, such as the higher the I_D/I_G ratio is, the lower the crystallinity. The I_D/I_G ratio of CSB (1.012) was found to be smaller than that of Vulcan XC-72 carbon (1.174), suggesting that CSB had a good graphitic crystalline structure than Vulcan XC-72 carbon. Compared with that of Vulcan XC-72 carbon, the *G* bands of the CSB shifted positively, where such shifts originate from the doping of nitrogen atom into carbon [22].

The contents of C, N and O in the CSB were determined by elemental analysis. The results indicates the mass contents of C, N and O are 87.7 %, 5.6 % and 6.7 % respectively.

The XRD patterns of the CSB and the Vulcan XC-72 are shown in Figure 3. In the XRD patterns of CSB, one peak at around $2\theta \approx 23^{\circ}$ is observed in both samples, which is attributed to the reflections of the (0 0 2) plane of the graphitic structure [23]. No impurity peaks were observed, such as traces of inorganic calcium salt, suggesting that the inorganic impurities were removed during the various acid washing steps. The broad and weak diffraction peaks of the (0 0 2) plane indicate that graphite with amorphous structure was formed after the sheep bones was carbonized with KOH [24]. Compared to the XRD pattern for Vulcan XC-72, the obvious left shift of the C (0 0 2) peaks for CSB, indicates an increase of the *d*-spacing of the C (0 0 2) plane caused by N atoms introduction into the structure.

The porous structures of the CSB were characterized by the nitrogen

adsorption-desorption isotherms (Figure 4). The isotherms of the CSB exhibit *Langmuir I* at low relative pressures and *type IV* sorption isotherm at relatively high pressures according to *IUPAC*, indicating the existence of micropores and mesopores in the structure. The high N_2 sorption capacity indicates that the *as*-synthesized sample possesses a high surface area and pore volume as shown in Figure 4a. The corresponding pore size distributions revealed that the CSB possesses hierarchical porosities ranging from micropores to mesopores. The CSB possesses a huge number of pores of various diameters in two main regions, namely: [0.8～2.0 nm] and [2.0～4.0 nm]. The Brunauer Emmett Teller (BET) surface area of CSB was found to be ~1,961 m^2g^{-1}, which is much larger than the previously reported carbon materials made from biomass (the literature findings are summarized in Table 1). High surface areas usually provide more active sites for catalytic reactions. The micropore surface area was also determined and found to be ~1,166 m^2g^{-1}. By calculating the ratio of the micropore surface area to the total surface area, a porosity of 59% was found for CSB, confirming a micropore structure.

To investigate the chemical composition and the chemical state of the CSB material, XPS analyses were conducted (Figure 5). From Figure 5a three typical XPS peaks for CSB are observed, corresponding to the binding energies of C *1s*, N *1s*, and O *1s*. It is widely accepted that nitrogen atoms can directly or indirectly enhance ORR on carbon electrodes. Figure 5b shows the high resolution spectrum of nitrogen *1s* peak, which can be de-convoluted into four peaks and can be assigned as pyridinic-*N* (398.8 eV), pyrrolic-*N* (400.3 eV), quaternary-*N* (401.5 eV) and the chemisorbed nitrogen oxide

species (402.2 eV) [33]. In addition, the atomic contents of pyridine-*N*, pyrrolic-*N*, quaternary-*N* and nitrogen oxide relative to the total N atoms are 27 %, 18%, 21 % and 36 % respectively. From the results, it was found that a considerable part of N species on CSB were in the form of pyridine-*N* and quaternary-*N*, which are considered to be the most active species for ORR [34].

Figure 6 shows the cyclic voltammograms (CVs) of carbon materials derived from sheep bone and commercial carbon black in nitrogen saturated 0.1 M KOH solution and at a scan rate of 50 mVs^{-1}. As shown in Figure 6a, CSB shows reversible curves with featureless wide voltammetric responses in nitrogen saturated solution, which are typical characteristics of heteroatom-doped carbon tested in N_2-saturated electrolyte [35]. Compared to Vulcan XC-72, the CV curves for CSB exhibits a quasi-rectangular shape, characteristic of *pseudo*-capacitive behaviour of N-doped carbons of high surface areas, facilitating charge dissemination [36]. Figure 6b displays the ORR activity of the CBS, Pt/C (10 wt.%) and Vulcan XC-72 by linear sweep voltammetry (LSV) using a RDE immersed in 0.1 M KOH aqueous solution saturated with O_2. It should be noted that LSVs indicated were obtained by using LSVs measured in O_2 saturated KOH solution minus the LSV gotten in N_2 saturated KOH solution in order to remove the capacitive contribution on LSV. As shown in Figure 6b, Vulcan XC-72 shows very low ORR activity in the KOH medium. LSV obtained on Vulcan XC-72 showed a reduction peak at around 0.76 V vs. RHE with no current plateau (limiting current), which is mainly due to the two-electron reduction reaction of O_2 to OOH^- [37]. Both LSVs of the commercial Pt/C and CSB show a sharp drop and rapidly

achieved saturation, indicating that ORR on both samples was a diffusion-controlled process via an efficient $4e^-$ transfer. After the potential is lower than 0.5V, the currents gradually drop with the potential, which probably caused by some side processes. The onset potential determined at a relatively small current density (-0.06 mA cm^{-2}) catalyzed by the CSB (0.97 V) shifts to more positive potential compared with the Pt/C (0.97 V) and XC-72 (0.76 V), and the current density at 0.87V ($I_{0.87V}$) of the ORR on CSB (0.35 mA cm^{-2}) is also larger than that of the Pt/C (0.35 mA cm^{-2}) and XC-72 (0.021 mA cm^{-2}) in the kinetic-diffusion controlled potential range, which indicates a higher kinetic activity for the CSB. It is worth noting that the ORR onset potential and the current density at 0.87V ($I_{0.87V}$) for CSB is more positive than those listed in Table 1. These results indicate that CSB is an excellent *N*-doped carbon catalyst for ORR in alkaline solution.

The LSV curves (currents normalized to the BET surface areas) of Pt/C and CBS were also calculated and shown in Figure 6c. As shown in Figure 6c, the current density of CBS is much lower than that of Pt/C, which shows that the Pt is much more active than CBS. However, Figure 6b shows that the ORR activity for carbon and Pt are so close, which only because the CBS has much higher specific surface area. Both direct and reverse scans for ORR on CBS and Pt/C were also carried out in oxygen-saturated 0.1 M KOH solution (Figure 6d). There is a clear direct and reverse scan polarization loop on Pt/C, but this loop is not found on CBS. In the case of Pt/C, its surface is covered with adsorbed surface oxide species which can block the adsorption of oxygen, resulting in a lower ORR current and forming a hysteresis loop.

However, the mechanism of ORR on carbon materials is different from Pt-based catalysts. The adsorbed surface species on carbon materials is $-OH_{ads}$, which does not block the adsorption of oxygen and can actually facilitate the charge transfer [38]. Therefore, no hysteresis loop will be observed on the carbon materials.

To investigate the number of electrons transferred per O_2 molecule on the CSB in the ORR, the reaction kinetic parameters were studied using the rotating disc voltammetry method at rotation speeds ranging from 400 to 2,500 rpm in O_2-saturated 0.1 mol L^{-1} KOH solution. RDE current-potential curves at various rotating speeds are shown in Figure 7a. The number of electrons transferred (n) in the ORR on CSB was determined using the Koutecky-Levich (K-L) equation [33]:

$$\frac{1}{j} = \frac{1}{j_k} + \frac{1}{B\omega^{0.5}} \quad (1)$$

where j is the measured current density, j_k is the kinetic current, ϖ is the rotation speed and B is the slope of K-L plots which is obtained from Figure 7b based on the Levich equation [39]:

$$B = 0.2nF(D_{O_2})^{2/3}v^{-1/6}C_{O_2} \quad (2)$$

where n is the number of electrons transferred in the reduction of one O_2 molecule in the ORR, F is the Faraday constant (F = 96,485 C mol^{-1}), D_{O_2} is the diffusion coefficient of O_2 in 0.1 mol L^{-1} KOH (D_{O_2} = 1.9×10^{-5} cm^2 s^{-1}), C_{O_2} is the bulk concentration of O_2 in the electrolyte (C_{O_2} = 1.2×10^{-6} mol cm^{-3}), and v is the kinematic viscosity of the electrolyte (v = 0.01 cm^2 s^{-1}). Here, the constant 0.2 is used when the rotation speed is expressed in rpm. The kinetic current densities of CBS and Pt/C measured at the potential of 0.6V were -3.74 and -3.79 respectively. According to

the equation, the number of electrons transferred can be calculated from the slope of i^{-1} plotted vs. $\omega^{-1/2}$. The average n values obtained from the curves were found to be ~3.85, suggesting that the ORR on CSB mainly proceeds via a $4e^-$ transfer mechanism [40]. This finding indicates an efficient four-electron transfer reaction occurring on CBS to reduce oxygen directly to OH^-, which is similar to the effective oxygen reduction process occurring on highly active commercial Pt/C electrode.

The electrocatalytic stability is another very important parameter for cathode electrocatalysts. The ORR stability of CSB and Pt/C was assessed by potential cycling in the range 0.165 to 1.16 V vs. RHE. Figure 8 shows the LSVs (ω = 1,600 rpm; scan rate = 5 mV s^{-1}) of CSB and Pt/C electrodes in 0.1 M KOH solution saturated with O_2 at initial and 1,000th cycles. From the LSVs, it is possible to evaluate the stability of the materials by determining the half-wave potential ($E_{1/2}$). It can be seen from Figure 8 that the half-wave potential decreases by ~43 mV and ~62 mV after the 1,000th cycles for CSB and Pt/C respectively, indicating that the CSB has a better stability in ORR than commercial Pt/C catalyst.

Conclusions

A high surface area and porous carbon material with high ORR activity was successfully produced from sheep bone via a facile and low-cost method. BET specific surface area of CSB was found to be ~1,961 m^2g^{-1}. Compared with the Pt/C (10 wt.%), the CSB exhibits a comparable ORR electrocatalytic activities in KOH solution. XPS results show that most of the N species on CSB were in the form of pyridine-N and quaternary-N, which are considered to be the active species for the

ORR. CSB is therefore a promising alternative material to commercial Pt/C for ORR in alkaline solution due to its higher activity, much better stability, low cost and easy synthesis.

Acknowledgments

The authors would like to thank the Youth Fund Promotion Plan of Northwest Normal University (NWNU-LKQN-14-20) and National Natural Science Foundation of China (21363022, and 51362027), Shenzhen Innovation Program JCYJ20140418095735600 for financially supporting this work.

References

1. Geng D, Chen Y, Chen Y, Li Y, Li R, Sun X, Ye S, Knights S (2011) High oxygen-reduction activity and durability of nitrogen-doped graphene. Energy Environ Sci 4 (3):760-764

2. Yang M, Van Wassen AR, Guarecuco R, Abruna HD, DiSalvo FJ (2013) Nano-structured ternary niobium titanium nitrides as durable non-carbon supports for oxygen reduction reaction. Chem Commun 49 (92):10853-10855

3. Sharma S, Pollet BG (2012) Support materials for PEMFC and DMFC electrocatalysts—A review. J Power Sources 208:96-119

4. Wang R, Wang K, Wang H, Wang Q, Key J, Linkov V, Ji S (2013) Nitrogen-doped carbon coated ZrO2 as a support for Pt nanoparticles in the oxygen reduction reaction. Int J Hydrogen Energy 38 (14):5783-5788

5. Huang L, Han Y, Dong S (2016) Highly-branched mesoporous Au-Pd-Pt trimetallic nanoflowers blooming on reduced graphene oxide as oxygen reduction electrocatalyst.

Chem Commun. 52: 8659-8662

6. Zhang Z, Li H, Yang Y, Key J, Ji S, Ma Y, Wang H, Wang R (2015) Cow dung-derived nitrogen-doped carbon as a cost effective, high activity, oxygen reduction electrocatalyst. RSC Adv 5 (34):27112-27119

7. Liang Y, Wang H, Zhou J, Li Y, Wang J, Regier T, Dai H (2012) Covalent Hybrid of Spinel Manganese–Cobalt Oxide and Graphene as Advanced Oxygen Reduction Electrocatalysts. J Am Chem Soc 134 (7):3517-3523.

8. Toh RJ, Eng AYS, Sofer Z, Sedmidubsky D, Pumera M (2015) Ternary Transition Metal Oxide Nanoparticles with Spinel Structure for the Oxygen Reduction Reaction. ChemElectroChem 2 (7):982-987

9. Wu Z-S, Yang S, Sun Y, Parvez K, Feng X, Müllen K (2012) 3D Nitrogen-Doped Graphene Aerogel-Supported Fe3O4 Nanoparticles as Efficient Electrocatalysts for the Oxygen Reduction Reaction. J Am Chem Soc 134 (22):9082-9085

10. Lin Z, Waller GH, Liu Y, Liu M, Wong C-p (2013) 3D Nitrogen-doped graphene prepared by pyrolysis of graphene oxide with polypyrrole for electrocatalysis of oxygen reduction reaction. Nano Energy 2 (2):241-248

11. Yang L, Jiang S, Zhao Y, Zhu L, Chen S, Wang X, Wu Q, Ma J, Ma Y, Hu Z (2011) Boron-Doped Carbon Nanotubes as Metal-Free Electrocatalysts for the Oxygen Reduction Reaction. Angew Chem Int Ed 123 (31):7270-7273.

12. Liu S-H, Wu M-T, Lai Y-H, Chiang C-C, Yu N, Liu S-B (2011) Fabrication and electrocatalytic performance of highly stable and active platinum nanoparticles supported on nitrogen-doped ordered mesoporous carbons for oxygen reduction

reaction. J Mater Chem A 21 (33):12489-12496

13. Han W-Q, Kohler-Redlich P, Seeger T, Ernst F, Rühle M, Grobert N, Hsu W-K, Chang B-H, Zhu Y-Q, Kroto HW, Walton DRM, Terrones M, Terrones H (2000) Aligned CN[sub x] nanotubes by pyrolysis of ferrocene/C[sub 60] under NH[sub 3] atmosphere. Appl Phys Lett 77 (12):1807.

14. Nath M, Satishkumar BC, Govindaraj A, Vinod CP, Rao CNR (2000) Production of bundles of aligned carbon and carbon–nitrogen nanotubes by the pyrolysis of precursors on silica-supported iron and cobalt catalysts. Chem Phys Lett 322 (5):333-340.

15. Yang Z, Xia Y, Mokaya R (2005) Aligned N-Doped Carbon Nanotube Bundles Prepared via CVD Using Zeolite Substrates. Chem Mater 17 (17):4502-4508.

16. Liu R, Wu D, Feng X, Müllen K (2010) Nitrogen-Doped Ordered Mesoporous Graphitic Arrays with High Electrocatalytic Activity for Oxygen Reduction. Angew Chem Int Ed 122 (14):2619-2623.

17. Xu X, Li Y, Gong Y, Zhang P, Li H, Wang Y (2012) Synthesis of Palladium Nanoparticles Supported on Mesoporous N-Doped Carbon and Their Catalytic Ability for Biofuel Upgrade. J Am Chem Soc 134 (41):16987-16990.

18. Liu G, Li X, Ganesan P, Popov BN (2009) Development of non-precious metal oxygen-reduction catalysts for PEM fuel cells based on N-doped ordered porous carbon. Appl Catal B: Environ 93 (1–2):156-165.

19. Kim ND, Kim W, Joo JB, Oh S, Kim P, Kim Y, Yi J (2008) Electrochemical capacitor performance of N-doped mesoporous carbons prepared by ammoxidation. J

Power Sources 180 (1):671-675. 20. Yang Q-H, Hou P-X, Unno M, Yamauchi S, Saito R, Kyotani T (2005) Dual Raman Features of Double Coaxial Carbon Nanotubes with N-Doped and B-Doped Multiwalls. Nano Letters 5 (12):2465-2469.

21. Chen Z, Higgins D, Tao H, Hsu RS, Chen Z (2009) Highly Active Nitrogen-Doped Carbon Nanotubes for Oxygen Reduction Reaction in Fuel Cell Applications. J Phys Chem C 113 (49):21008-21013.

22. He X, Li R, Qiu J, Xie K, Ling P, Yu M, Zhang X, Zheng M (2012) Synthesis of mesoporous carbons for supercapacitors from coal tar pitch by coupling microwave-assisted KOH activation with a MgO template. Carbon 50 (13):4911-4921.

23. Zhou T, Wang H, Ji S, Linkov V, Wang R (2014) Soybean-derived mesoporous carbon as an effective catalyst support for electrooxidation of methanol. J Power Sources 248:427-433.

24. Wang H, Zhang X, Wang R, Ji S, Wang W, Wang Q, Lei Z (2011) Amorphous CoSn alloys decorated by Pt as high efficiency electrocatalysts for ethanol oxidation. J Power Sources 196 (19):8000-8003.

25. Ma Y, Zhao J, Zhang L, Zhao Y, Fan Q, Li Xa, Hu Z, Huang W (2011) The production of carbon microtubes by the carbonization of catkins and their use in the oxygen reduction reaction. Carbon 49 (15):5292-5297.

26. Lu J, Bo X, Wang H, Guo L (2013) Nitrogen-doped ordered mesoporous carbons synthesized from honey as metal-free catalyst for oxygen reduction reaction. Electrochim Acta 108:10-16.

27. Wang R, Wang K, Wang Z, Song H, Wang H, Ji S (2015) Pig bones derived N-doped carbon with multi-level pores as electrocatalyst for oxygen reduction. J Power Sources 297:295-301.

28. Zhang J, Wu S, Chen X, Pan M, Mu S (2014) Egg derived nitrogen-self-doped carbon/carbon nanotube hybrids as noble-metal-free catalysts for oxygen reduction. J Power Sources 271:522-529.

29. Wang H, Wang K, Song H, Li H, Ji S, Wang Z, Li S, Wang R (2015) N-doped porous carbon material made from fish-bones and its highly electrocatalytic performance in the oxygen reduction reaction. RSC Adv 5 (60):48965-48970.

30. Zhu H, Yin J, Wang X, Wang H, Yang X (2013) Microorganism-Derived Heteroatom-Doped Carbon Materials for Oxygen Reduction and Supercapacitors. Adv Func Mater 23 (10):1305-1312.

31. Song H, Li H, Wang H, Key J, Ji S, Mao X, Wang R (2014) Chicken bone-derived N-doped porous carbon materials as an oxygen reduction electrocatalyst. Electrochim Acta 147:520-526.

32. Liu F, Peng H, Qiao X, Fu Z, Huang P, Liao S (2014) High-performance doped carbon electrocatalyst derived from soybean biomass and promoted by zinc chloride. Int J Hydrogen Energy 39 (19):10128-10134.

33. Wang K, Wang H, Ji S, Feng H, Linkov V, Wang R (2013) Biomass-derived activated carbon as high-performance non-precious electrocatalyst for oxygen reduction. RSC Adv 3 (30):12039.

34. Zhang Z, Li H, Yang Y, Key J, Ji S, Ma Y, Wang H, Wang R (2015) Cow

dung-derived nitrogen-doped carbon as a cost effective, high activity, oxygen reduction electrocatalyst. RSC Adv 5 (34):27112-27119.

35. Wang R, Wang H, Zhou T, Key J, Ma Y, Zhang Z, Wang Q, Ji S (2015) The enhanced electrocatalytic activity of okara-derived N-doped mesoporous carbon for oxygen reduction reaction. J Power Sources 274:741-747.

36. Zheng Y, Jiao Y, Chen J, Liu J, Liang J, Du A, Zhang W, Zhu Z, Smith SC, Jaroniec M, Lu GQ, Qiao SZ (2011) Nanoporous graphitic-C3N4@carbon metal-free electrocatalysts for highly efficient oxygen reduction. J Am Chem Soc 133 (50):20116-20119.

37. Wen Z, Ci S, Zhang F, Feng X, Cui S, Mao S, Luo S, He Z, Chen J (2012) Nitrogen-enriched core-shell structured Fe/Fe(3)C-C nanorods as advanced electrocatalysts for oxygen reduction reaction. Adv Mater 24 (11):1399-1404.

38. Wan K, Yu Z, Li X, Liu M, Yang G, Piao J, Liang Z (2015) pH Effect on Electrochemistry of Nitrogen-Doped Carbon Catalyst for Oxygen Reduction Reaction. ACS Catal 5: 4325-4332.

39. Kang J, Wang H, Ji S, Key J, Wang R (2014) Synergy among manganese, nitrogen and carbon to improve the catalytic activity for oxygen reduction reaction. J Power Sources 251 (0):363-369.

40. Ma Y, Wang R, Wang H, Key J, Ji S (2015) Control of MnO2 nanocrystal shape from tremella to nanobelt for ehancement of the oxygen reduction reaction activity. J Power Sources 280:526-532.

Response Letter

Dear Editors and Reviewers:

We are truly grateful for your comments and thoughtful suggestions. As such, we have made careful modifications to the manuscript. Changes to the text regarding specific queries of the reviewers are in red colored text. Please find our responses to the comments and queries below:

Reviewer #2: The authors improved some points, but misunderstood my principle comments concerning the treatment of ORR data.

(1) Both direct and reverse scans should be shown, to see whether hysteresis exists for the catalysts under comparison.

Response: Thanks for your suggestion. Both direct and reverse scans for CSB and Pt/C were tested and present in Fig. 6d. There is a hysteresis loop on the Pt/C catalysts, but hysteresis loop is not found on the CBS. According to paper published on ACS Catalysis (Wan *et al.* pH Effect on Electrochemistry of Nitrogen-Doped Carbon Catalyst for Oxygen Reduction Reaction, ACS Catalysis, 2015, 5, 4325-4332), the positive-going and negative-going polarization loop was found on the Pt/C catalyst. For the Pt/C catalyst, it is acknowledged that the coverage of adsorbed surface oxide species has a pronounced effect on the ORR performance. Fully covered oxide species can retard the adsorption of oxygen and, thus, lower the ORR polarization

curve. As such, the hysteresis loop in the cyclic polarization curve can be qualitatively understood by considering the coverage of the adsorbed oxide species. However, the case is different for the carbon catalyst. On the carbon materials, the ORR proceeds in a redox-mediated mechanism, in which the adsorbed surface species ($-OH_{ads}$) does not block the charge transfer but acts as the bridge to facilitate the charge transfer. As such, the hysteresis loop behavior is not observed in the carbon-based catalyst. We also spent a lot of time to prepare many other N-doped carbon materials, and did direct and reverse scans for them. All of carbon materials don't show the hysteresis loop.

(2) I assumed that some current is spent for by-side process because at potentials below 0.5 V (Fig. 6b) the current on carbon (black curve) exceeds the limiting diffusion current. Nobody knows, probably the same by-side process occurs at more positive potentials as well, and contributes to the current which the authors treat as purely ORR current.

Response: Thanks for your comment. At potentials below 0.5 V (Fig. 6b) and at more positive potentials the current on carbon (black curve) exceeds the limiting diffusion current, which probably caused by some side processes. In the revised manuscript, we modified our description to avoid contributing the current to purely ORR current.

(3) To compare with Pt and other materials, the following steps are necessary:

- to calculate the kinetic current at fixed potential,

Response: Thanks for your comment. The kinetic current density (j_k) in the ORR on CSB and Pt/C were calculated using the Koutecky-Levich (K-L) equation:

$$\frac{1}{j} = \frac{1}{j_k} + \frac{1}{B\omega^{0.5}}$$

where j is the measured current density, ϖ is the rotation speed, B is the slope of K-L plots which is obtained from Figure 7b. The kinetic current densities of CBS and Pt/C measured at the potential of 0.6V were -3.74 and -3.79 respectively. Corresponding modifications have been made in the revised manuscript.

- to normalize this current to the true surface area taking into account the loading.

I suspect that now the values reported by the authors correspond to more straightforward procedure because the ORR waves for carbon and Pt are so close only because carbon has much higher specific surface area. Note that Pt content in the sample is only 10%, so Pt is surely many orders more active. There is also no sense to compare mixed currents at certain potential instead of kinetic currents, because the former depend on hydrodynamic mode (rotation rate).

Response: Thanks for this comment. The current normalized to the BET surface areas was added in Fig. 6c in the modified paper. As shown in Fig. 6c, the current density of CBS is much lower than that of Pt/C, which shows that the Pt is much more active than carbon materials. However, Fig. 6b shows that the ORR activity for carbon and

Pt are so close, which only because the CBS has much higher specific surface area.

In the next revision, the authors should avoid the excess accuracy. It is evident that subtraction of curves in N2 saturated solution and recalculation to kinetic current can not provide the accuracy of three significant digits.

Response: Thanks for your suggestion; these figures were accurate to two decimal places in the revised paper.

Figures:

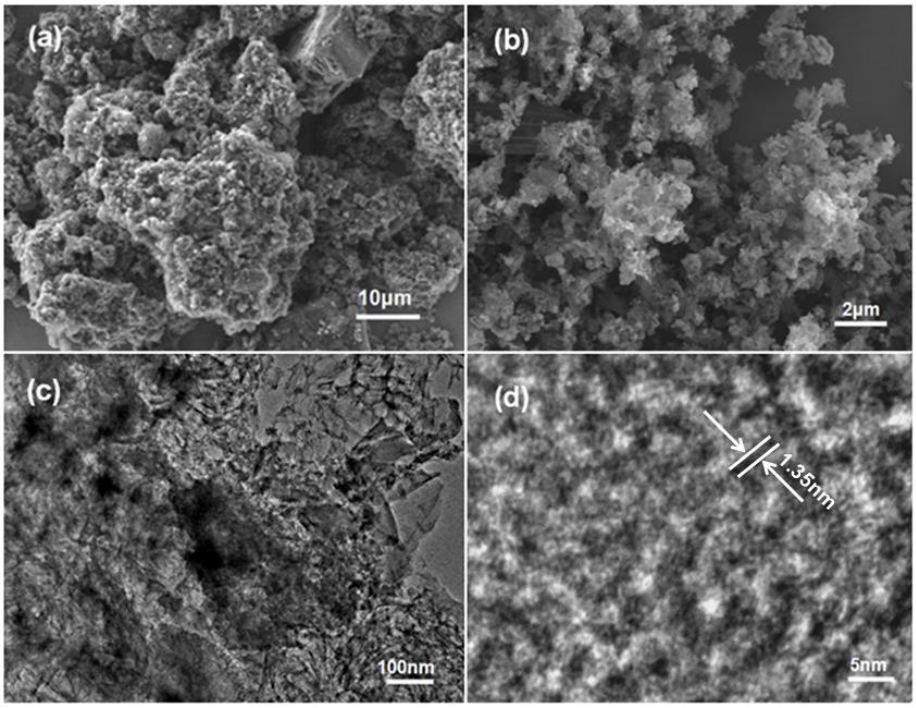

Figure 1. SEM (a) images of the carbon surfacebefore chemical activation. SEM (b),TEM (c) and HR-TEM (d) images ofthe carbon surface after chemical activation.

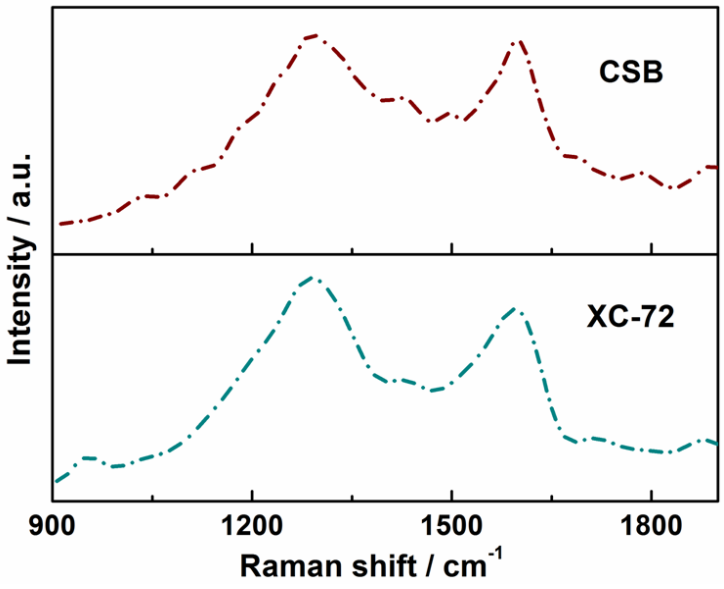

Figure 2. Raman spectra of CSB and XC-72 carbon

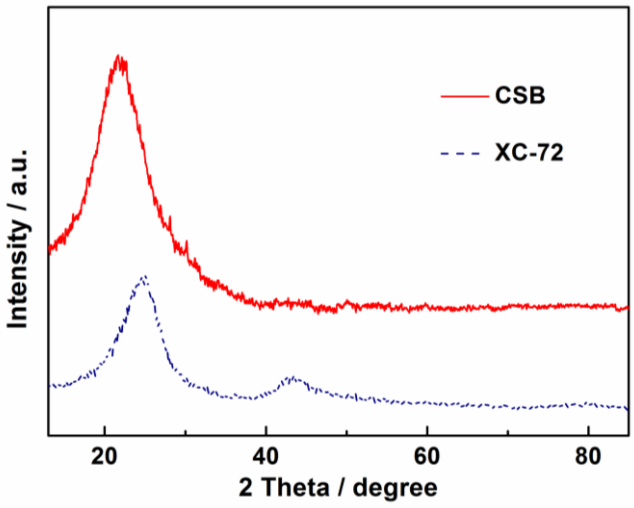

Figure3.The XRD patterns of CSB and XC-72.

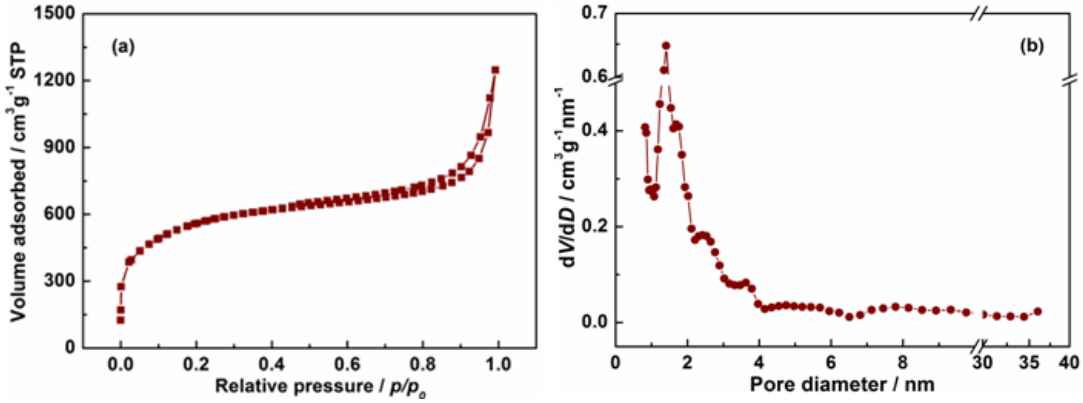

Figure 4. N_2 adsorption-desorption isotherms (a) and pore size distribution (b) of CSB and Vulcan XC-72.

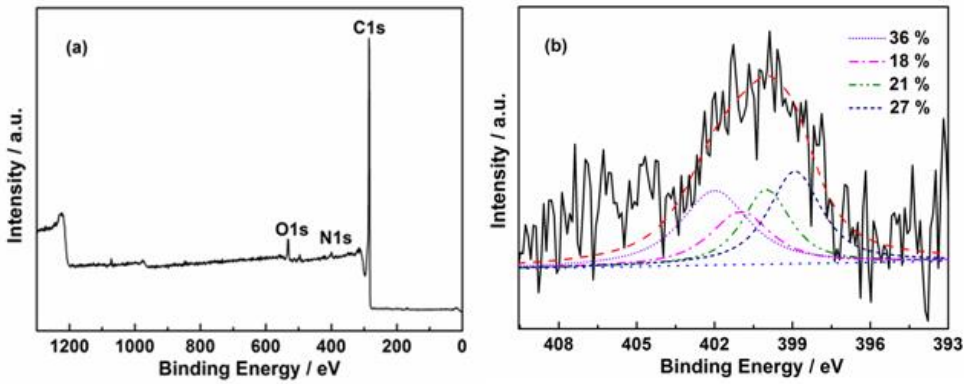

Figure 5 (a) XPS survey spectrum of CSB; (b) High resolution XPS spectrum at N*1s* region of CSB.

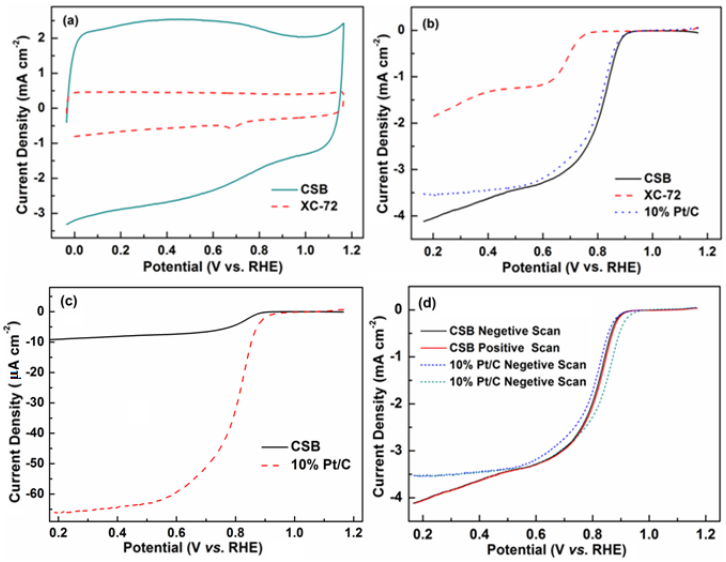

Figure 6. (a) Cyclic voltammograms of CSB and XC-72 in N_2-saturated 0.1 M KOH solution; scan rate: 50 mV s^{-1}; (b) LSV curves for ORR in oxygen-saturated 0.1 M KOH solution on CSB, Pt/C and XC-72; (c) LSV curves (current normalized to BET surface area) for ORR in oxygen-saturated 0.1 M KOH solution on CSB and Pt/C; (d) Polarization curves of Pt/C and CSB in oxygen-saturated 0.1 M KOH solution; rotating rate: 1,600 rpm; sweep rate 5mV s^{-1}.

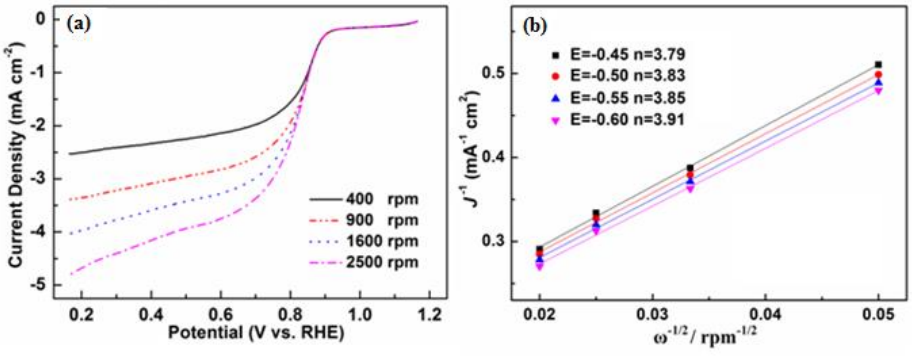

Figure 7. (a) Polarization curves for ORR in O_2 saturated 0.1 M KOH solution on CSB electrode at various rotation speeds; (b) The Koutecky-Levich (K-L) plots for ORR derived from Figure 6a. All catalysts loadings are 0.20 mg cm^{-2}.

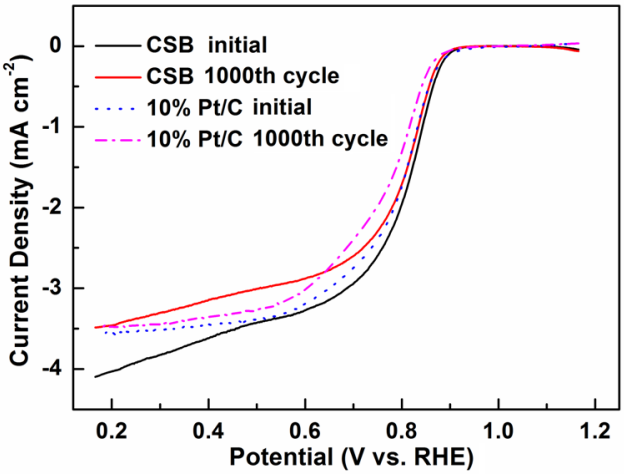

Figure 8. Linear sweep voltammograms (LSV) CSB and commercial Pt/C (10%) before and afterthe 1,000thcycles in O_2-saturated 0.1 M KOH solution at a scan rate of 5 mV s^{-1}.

Table:

Table 1. Summary of values derived from BET in Figure 4 and LSV in Fig.6(b) vs.results from anotherreferences.

Catalyst	Precursors	The catalyst loading (mg cm^{-2})	BET surface area (m^2 g^{-1})	Onset potential for ORR (V *vs.* RHE)	$-I_{0.87v}$ (mA cm^{-2})	Ref.
CSB	Sheep bone	0.20	1,961	0.977	0.353	This work
CMT-950	Catkin	0.20	257	0.775[a]	0.015[b]	[25]
N-OMC-800	Honey	0.14	1,273	0.835	0.167[a]	[26]
CS_1	Pig bone	0.02	543	0.146	0.097	[27]
CE	Egg	0.30	975	0.930	0.27[b]	[28]
CFB	Fish bone	0.20	563	0.968	0.255	[29]
BP-800	Bacillus subtilis	1.0	1,578	0.785	-	[30]
CCB_2	Chicken bone	0.20	769	0.7053 [b]	0.153[b]	[31]
BCZA-900-1/2	Soybean	0.10	949	0.945	0.78[b]	[32]

[a]Electrolyte: 1 mol L^{-1}NaOH; [b]The value estimated derived from the figure.